Quantitative characterization of X-ray lenses from two fabrication techniques with grating interferometry

Frieder J. Koch,[1,*] Carsten Detlefs,[2] Tobias J. Schröter,[1] Danays Kunka,[1] Arndt Last,[1] and Jürgen Mohr[1]

[1]*Institute of Microstructure Technology, Karlsruhe Institute of Technology, 76344 Eggenstein-Leopoldshafen, Germany*
[2]*European Synchrotron Radiation Facility, Grenoble 38000, France*
[*]frieder.koch@kit.edu

Abstract: Refractive X-ray lenses are in use at a large number of synchrotron experiments. Several materials and fabrication techniques are available for their production, each having their own strengths and drawbacks. We present a grating interferometer for the quantitative analysis of single refractive X-ray lenses and employ it for the study of a beryllium point focus lens and a polymer line focus lens, highlighting the differences in the outcome of the fabrication methods. The residuals of a line fit to the phase gradient are used to quantify local lens defects, while shape aberrations are quantified by the decomposition of the retrieved wavefront phase profile into either Zernike or Legendre polynomials, depending on the focus and aperture shape. While the polymer lens shows better material homogeneity, the beryllium lens shows higher shape accuracy.

References and links

1. A. Snigirev, V. Kohn, I. Snigireva, and B. Lengeler, "A compound refractive lens for focusing high-energy X-rays," Nature **384**(6604), 49–51 (1996).
2. T. Roth, L. Helfen, J. Hallmann, L. Samoylova, P. Kwaśniewski, B. Lengeler, and A. Madsen, "X-ray laminography and SAXS on beryllium grades and lenses and wavefront propagation through imperfect compound refractive lenses," Proc. SPIE **9207**, 920702 (2014).
3. T. Weitkamp, B. Nöhammer, A. Diaz, C. David, and E. Ziegler, "X-ray wavefront analysis and optics characterization with a grating interferometer," Appl. Phys. Lett. **86**(5), 054101 (2005).
4. S. Rutishauser, I. Zanette, T. Weitkamp, T. Donath, and C. David, "At-wavelength characterization of refractive x-ray lenses using a two-dimensional grating interferometer," Appl. Phys. Lett. **99**(22), 221104 (2011).
5. K. S. Morgan, D. M. Paganin, and K. K. W. Siu, "Quantitative x-ray phase-contrast imaging using a single grating of comparable pitch to sample feature size," Opt. Lett. **36**(1), 55–57 (2011).
6. H. H. Wen, E. E. Bennett, R. Kopace, A. F. Stein, and V. Pai, "Single-shot x-ray differential phase-contrast and diffraction imaging using two-dimensional transmission gratings," Opt. Lett. **35**(12), 1932–1934 (2010).
7. P. Zhou and J. H. Burge, "Analysis of wavefront propagation using the Talbot effect," Appl. Opt. **49**(28), 5351–5359 (2010).
8. W. Yashiro, S. Harasse, A. Takeuchi, Y. Suzuki, and A. Momose, "Hard-x-ray phase-imaging microscopy using the self-imaging phenomenon of a transmission grating," Phys. Rev. A **82**(4), 043822 (2010).
9. F. Uhlén, J. Rahomäki, D. Nilsson, F. Seiboth, C. Sanz, U. Wagner, C. Rau, C. G. Schroer, and U. Vogt, "Ronchi test for characterization of X-ray nanofocusing optics and beamlines," J. Synchrotron Radiat. **21**(5), 1105–1109 (2014).
10. V. Nazmov, E. Reznikova, J. Mohr, A. Snigirev, I. Snigireva, S. Achenbach, and V. Saile, "Fabrication and preliminary testing of X-ray lenses in thick SU-8 resist layers," Microsyst. Technol. **10**(10), 716–721 (2004).
11. F. Pfeiffer, M. Bech, O. Bunk, P. Kraft, E. F. Eikenberry, Ch. Brönnimann, C. Grünzweig, and C. David, "Hard-X-ray dark-field imaging using a grating interferometer," Nat. Mater. **7**(2), 134–137 (2008).
12. C. Kottler, C. David, F. Pfeiffer, and O. Bunk, "A two-directional approach for grating based differential phase contrast imaging using hard x-rays," Opt. Express **15**(3), 1175–1181 (2007).
13. F. Zernike, "Beugungstheorie des Schneidenverfahrens und seiner verbesserten Form, der

Phasenkontrastmethode," Physica **1**(7–12), 689–704 (1934).
14. J. Ye, Z. Gao, S. Wang, J. Cheng, W. Wang, and W. Sun, "Comparative assessment of orthogonal polynomials for wavefront reconstruction over the square aperture," J. Opt. Soc. Am. A **31**(10), 2304–2311 (2014).
15. A. Last, O. Márkus, S. Georgi, and J. Mohr, "Röntgenoptische Messung des Seitenwandwinkels direktlithografischer refraktiver Röntgenlinsen," in MikroSystemTechnik Kongress (2015).
16. M. Engelhardt, J. Baumann, M. Schuster, C. Kottler, F. Pfeiffer, O. Bunk, and C. David, "Inspection of refractive X-ray lenses using high-resolution differential phase contrast imaging with a microfocus X-ray source," Rev. Sci. Instrum. **78**(9), 093707 (2007).

1. Introduction

Compound refractive X-ray lenses (CRLs [1]) are commonly used at synchrotrons as optics to produce micro- and nanobeams, and as objectives in full field microscopy experiments. The key to achieving the high spatial resolution desired in these experiments is the quality of the optics involved. Common materials for CRLs are beryllium, diamond, aluminum, silicon and polymers. The fabrication processes used for these materials differ significantly, thus different defects and aberrations are to be expected.

In practice, focusing optics are often characterized in terms of the achieved size and shape of the focal spot. While this is an easy way to get an impression of lens quality, it only provides limited information on the lens and offers little feedback for improving the lens production. Scanning electron microscopy is a useful tool to inspect the surface quality of a lens, but provides limited quantitative information about shape errors, particularly for discrete lens elements (rather than lithographically-produced lens arrays). X-ray radiography can reveal defects inside a lens but is severely limited for the inspection of lenses made from materials with low X-ray absorption, such as beryllium or polymers. Laminography or computed tomography (CT) can provide a 3d picture of the lens shape and reveal voids and inclusions in the material [2], but they are time consuming techniques unsuited for routine quality control.

X-ray grating interferometry is a very efficient and rapid method for obtaining an image of the wavefront phase gradient. A grating is used to impose a periodic phase shift onto the incoming wavefront. The resulting interference pattern downstream is altered by the sample, and compared to a reference scan without sample. As it can be readily employed for materials with very weak absorption, it is a valuable tool for the characterization of refractive optics and can be used for the quantitative analysis of X-ray lenses [3,4].

We report on the implementation of a high resolution, single grating interferometer for the test of refractive lenses performed at the beamline ID06 of the ESRF. Using a high resolution detector in combination with a larger grating period enables us to directly resolve the interference pattern without an analyzer grating. This greatly simplifies the alignment such that the set-up and method can be used as a routine analysis tool. Additionally, we extended the analysis scheme to use Legendre polynomials to characterize shape errors of line focus lenses. In this work the interferometer was employed to test point focus lenses made from beryllium, and line focus lenses from SU-8 based polymer.

2. Experimental setup

Using the Si(111) monochromator at the ESRF beamline ID06, 17 keV X-rays were selected from the undulator source. A single line grating of pitch $p = 10$ µm with 3 µm high Ni lines, providing a phase shift of $\pi/2$, was placed ~56 m downstream of the source. The grating was mounted on a piezo scanner with lines oriented horizontally to make best use of the coherence of the asymmetric source at ID06 (size 415(h) x 8.6(v) µm^2 rms). A pco.2000 camera mounted behind a scintillator and microscope objective was used for detection, the effective pixel size was 0.74 µm. This was sufficient to directly resolve the interference pattern created by the grating, enabling the use of single shot measurements, in contrast to the more commonly used method of scanning an analyzer grating through the interference pattern and measuring the resulting Moiré pattern [3]. However, techniques for single shot analysis either

require a large pitch to feature size ratio [5] or sacrifice resolution [6], so phase stepping was employed to make use of the full detector resolution.

The interferometer was operated at two different distances which were chosen by scanning the grating along the optical axis and monitoring the contrast of the interference pattern. The two positions found to yield the best contrast were 0.2 and 0.7 times the Talbot distance of $z_T = 2p^2/\lambda = 2.74$ m. The discrepancy from the ideal fractional Talbot distances (0.25 z_T and 0.75 z_T) was traced back, using numerical simulations, to the fact that the duty cycle, defined as Ni width over period, of the phase grating was 0.42 instead of the usual 0.5, and the absorption in the Ni lines. The duty cycle was determined using pictures taken with an optical microscope

As the setup with a line grating is only sensitive to the phase gradient perpendicular to the grating lines, at least two scans have to be acquired to measure the full 2d phase gradient. This can be done by rotating either the sample or the gratings about the optical axis - the latter is equivalent to using a 2d grating [4]. For a highly anisotropic source such as ID06, however, this approach would yield very different sensitivities in the horizontal and vertical directions. Consequently, we chose to rotate the samples using a rotation stage. To perform scans at several azimuthal angles, the stage was moved and rotated about the transverse axes to align the rotation axis with the optical axis.

In order to analyze the position of the interference pattern, it has to be fully resolved by the detector pixels. This poses a limit to the minimal focal length of a lens to be analyzed with the interferometer. Assuming that one period p of the grating has to cover at least M pixels of size s on the detector to be reliably analyzed, simple geometric considerations yield the following formula for the minimal focal length f_{min}:

$$f_{min} = \frac{(d+a) \cdot p/Ms}{p/Ms - 1}.$$

Here, d denotes the distance from the grating to the detector, and $a = 80$ mm is the distance from the sample to the grating, which is assumed to be very small compared to d. There is, however, another restriction, because the converging beam after the lens changes the effective propagation distance L_e between grating and detector [7]:

$$L_e = \frac{(f-a) \cdot d}{f-a-d}.$$

For $L_e - d = z_T/4$, the amplitude contrast in the flat field is converted into pure phase contrast in the focused beam, and the fringe pattern is no longer observable. To avoid this and retain sufficient contrast for reliable data analysis, $L_e - d$ should be kept small, $L_e - d < z_T/8$.

For the setup described here, the resolution criterion yields a minimum focal length of 0.97 m for the shorter distance (0.2 z_T) and about 3 m for the longer distance (0.7 z_T); the restriction from the effective propagation distance is stronger, it limits the minimum focal length to 1.4 m for the shorter and 12.5 m for the longer distance. Hence the interferometer is optimal for lens types where each element is fabricated individually, such as imprinted Be, Al and Ni lenses, because single elements have large focal lengths. Lenses, where all elements are fabricated in a single step, such as SU-8 or Ni lenses from X-ray lithography, or Si lenses made by dry-etching techniques, can only be tested with some limitations. The limit of 1.4 m is a factor of 4.3 smaller than in previous experiments [4]. More general approaches can be used to characterize lenses of arbitrary focal length, for example investigating the image of the grating produced in a microscopy setup [8], or a Ronchi type interferometer [9]. However, in these techniques it is not possible to obtain a flat field image to characterize the incident wavefront without lens, which makes the determination of absolute, quantitative values difficult.

Two types of samples were tested in this study: Point focus beryllium lenses fabricated by imprinting [1] mounted in a steel frame, and line focus lenses fabricated by deep X-ray

lithography in an SU-8 based polymer on a silicon substrate [10]. Both lens types had a parabolic profile for focusing. In the following, the procedures and results are presented for two single lens element samples; a point focus beryllium lens of a circular aperture with 400 μm diameter and a nominal apex radius of 50 μm (focal length of 21 m at 17 keV), and a line focus SU-8 lens with an aperture of 1000 x 840 μm^2 and an apex radius of 300 μm (focal length 159 m). The Be lens was analyzed in the lower Talbot order, for the polymer lens, the higher Talbot order was chosen to increase sensitivity to smaller refraction angles.

3. Measurements

In order to obtain the amplitude and phase of the interference pattern for each pixel of the detector, the phase grating was scanned in 16 steps over one period, both with the sample in and out of the beam for reference. The resulting stack of images was analyzed using a method based on a fast Fourier transform (FFT) routine [11], where the intensity signal $I(x_g)$, with x_g as the grating position, in each pixel is approximated as the zeroth and first term of the Fourier series, $I^{r,s}(x_g) = a_0^{r,s} + a_1^{r,s} \cdot \cos(kx_g + \varphi^{r,s})$. The superscripts r and s stand for reference and sample, respectively. The transmission of the sample is then calculated as the ratio a_0^s / a_0^r. The ratio a_1^r / a_0^r is commonly referred to as the visibility V, and the ratio V_s / V_r as the dark field signal. The phase shift, $\Delta\varphi = \varphi^r - \varphi^s$, is of particular interest for assessing lens quality as it is directly proportional to the refraction angle as described below.

To recover the full phase gradient of an object, a minimum of two scans with a relative azimuthal angle of 90° is required. Registration of the scans was done by rotating the processed images and using cross-correlation of the transmission images to correct for the lateral offset. It is also possible to detect characteristic features such as circles or rectangles in the images and compare their positions. In practice, 4-12 scans, in pairs with 90° relative angle, were taken for each lens. This oversampling was used to identify artefacts in the final images. The resulting 2D phase gradient vectors were then projected along two reference directions. For the line focus lens these were chosen as the focusing and non-focusing directions. Figure 1 shows these two directions for the Be and the polymer lens. As expected there is no structure visible in the non-focusing direction of the polymer lens. On the left edge of the polymer lens images, stripes can be identified that show the edges of the field of view at different rotation angles. The value for the phase gradient is only accurate in the region where all the images overlap, which means that the upper left and lower left corner, indicated in Fig. 1 by fine dashed triangles, are not correctly characterized as they did not fit into the field of view at all rotational angles. In Fig. 1(A), two rings are visible, corresponding to the edges of the imprints from the two sides of the raw beryllium.
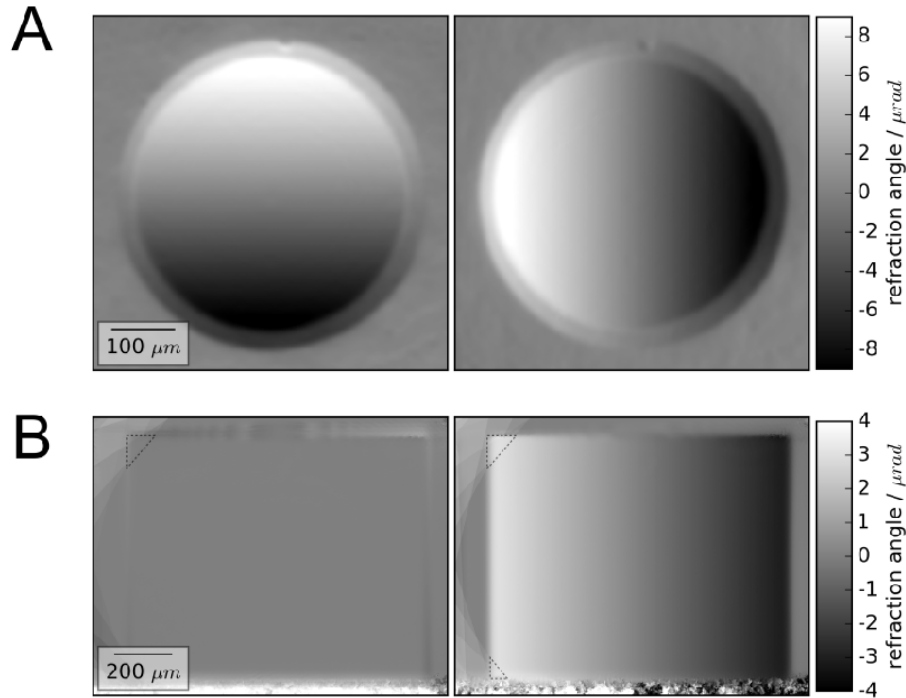
Fig. 1. Phase gradient in orthogonal directions for a beryllium point focus lens with apex radius 50 μm (A) and a polymer line focus lens with apex radius 300 μm (B). No structure is visible in the non-focusing direction of the line focus lens.

Let $S(x,y) = A(x,y) \cdot \exp(i\Phi(x,y))$ denote the complex amplitude of the wave field in the detector plane, propagating in z, and x the direction perpendicular to the grating lines. Then the phase shift $\Delta\varphi$ of the interference pattern obtained from the procedure described above is proportional to the wavefront phase gradient $\partial\Phi / \partial x$, and to the refraction angle α [2]:

$$\Delta\varphi = \frac{\lambda d}{p_{\text{det}}} \frac{\partial\Phi}{\partial x} = \alpha \frac{2\pi d}{p_{\text{det}}}.$$

Here, λ denotes the wavelength, d the distance from sample to detector and p_{det} the period of the interference pattern on the detector. For an ideal parabolic lens, the refractive angle is related to the focal length f and consequently the radius R of the apex of the parabola [1]:

$$\gamma \frac{\partial\alpha}{\partial x} = \frac{1}{f} = \frac{2\delta}{R}.$$

Here, δ denotes the refractive index decrement, and the factor γ describes the demagnification of the lens aperture from sample to detection plane, which can be calculated by determining the diameter l_d of the lens in the detector plane, and afterwards finding the shift of the interference pattern at the edges of the aperture. For a focusing lens, the total shift $\Delta\varphi_t$ between the edges is exactly the difference between the aperture diameter l in the lens plane and the detector plane, $l = l_d + \Delta\varphi_t$, which yields

$$\gamma = \frac{l_d}{l_d + \Delta\varphi_t}.$$

A linear fit to the refraction angle is used to determine f and R.

4. Data evaluation
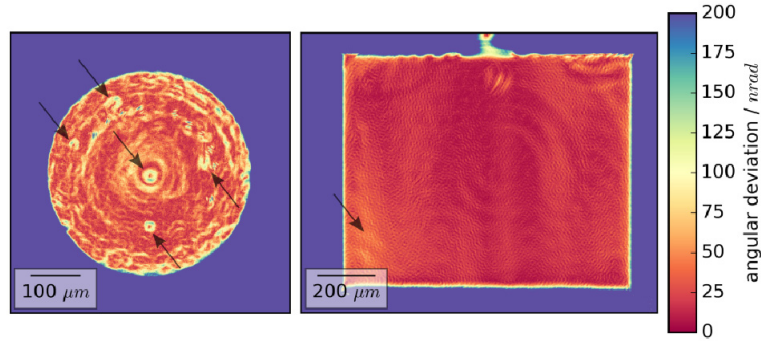
4.1 Local lens defects

Fig. 2. Deviation from ideal refraction angle for Be (left) and polymer lens (right). Plotted is the magnitude of the 2d angular deviation vector.

A plot of the residuals from the linear fit of the refraction angle reveals local lens defects. This can be done for both directions individually, pointing out the sign of the local deviation, or, for a better overview, in a combined plot showing the magnitude of the two-dimensional angular deviation vector. The angular deviation plots of Fig. 2 reveal different characteristics of local errors for the two lens types. First, the deviations found in the polymer lens are generally smaller (mean deviation inside aperture 18 nrad for the polymer lens vs. 47 nrad for the Be lens), but the values cannot be directly compared, as the focal length of the Be lens is approximately seven times smaller than of the polymer lens. At the same time, the latter's aperture is about 6.5 times larger.

The second striking difference between the two lens types is the localization of the defects. While in the Be lens, a larger deviation can be seen in the center and others off center at the positions indicated by the arrows, the defects in the polymer lens are smoother and spread over a larger area (e. g. in the lower left area of the aperture). This hints to different causes for the defects. The off-center defects in the Be lens are most likely due to material inhomogeneity, e. g. air bubbles or inclusions of other metals. A defect in the center was also seen by Rutishauser et al. for a lens with much larger radius of curvature [4] and is attributed to deformation of the imprinting tool during the fabrication process. In the polymer lens, there are no indications for local defects of this kind; the deviations instead seem to be related to errors in the shape, e. g. sidewall slope errors.

The structure of concentric circles seen in the deviation map of the polymer lens, as well as a higher spatial frequency oscillation are artifacts from beam instabilities; an artifact from a grating defect can be seen as a small defect in the Be lens repeating at ten azimuthal angles (see Appendix for more details).

4.2 Global defects and shape errors

In order to characterize low frequency lens defects such as spherical aberration or astigmatism, the wavefront phase profile was retrieved using a Fourier transformation based integration method [12]. The common method for the quantification of aberrations in point focus lenses with circular aperture is the decomposition of the measured wavefront S into Zernike polynomials Z_n^m, with n as the radial and m as the azimuthal degree [13], $S = \sum_{n,m} A_n^m \cdot Z_n^m$. These polynomials form an orthogonal base of the unit disc and can be identified with the common geometric lens aberrations. On discrete data sets like the pixelated images presented here, the polynomials are no longer strictly orthogonal. To minimize

crosstalk between coefficients, we first determined the largest term, subtracted this contribution from the data set, and then repeated the process until all coefficients had been determined.

The coefficients for the individual Zernike polynomials obtained with this procedure for the Be lens are listed in Table 1, in units of Beryllium thickness. The defocus term is a rotational paraboloid that corresponds, with a negative sign, to the shape of an ideal point focus lens. The aberrations measured are generally very small, all contributions of error terms are smaller than 1% of the desired defocus term A_2^0. The only notable contributions are spherical aberration, horizontal coma and some oblique astigmatism.

Table 1. Zernike Coefficients for the Point Focus Be Lens

Name	n, m	$A_n^m / \mu m$
Defocus	2, 0	−255.7
Oblique astigmatism	**2, −2**	**-0.21**
Vertical astigmatism	2, 2	0.04
Vertical coma	3, −1	−0.10
Horizontal coma	**3, 1**	**0.42**
Vertical trefoil	3, −3	−0.09
Oblique trefoil	3, 3	0.02
Primary spherical	**4, 0**	**0.76**
Vertical secondary astigmatism	4, 2	0.08
Oblique secondary astigmatism	4, −2	−0.08
Vertical quadrafoil	4, 4	−0.01
Oblique quadrafoil	4, −4	−0.05

While the Zernike polynomials provide a good representation of the wavefront after a point focus lens with circular aperture, they are unsuited for the polymer lens with its line focus and rectangular aperture. Several other orthogonal sets of polynomials are available for rectangular apertures, e.g. Chebyshev and Legendre polynomials or Zernike square polynomials [14]. As the Zernike square polynomials do not contain terms that are quadratic in only one spatial dimension, only the 2d Chebyshev and Legendre polynomials are well suited for the problem at hand. Both were applied, with the Legendre polynomials yielding a distinctively better representation of the wavefront when restricted to the first 15 terms.

The 2d Legendre polynomials $L_j(x, y)$ are constructed by multiplying the 1d Legendre polynomials P_n of degree n in x and y:

$$L_j(x, y) = P_n(x) \cdot P_m(y).$$

They fulfill the orthogonality condition as follows:

$$\int_{-1}^{1} \int_{-1}^{1} L_j(x, y) \cdot L_k(x, y) dx dy = 4 \cdot \delta_{jk},$$

with δ_{jk} as the Kronecker delta. The coefficients for the polymer lens were obtained using the same serial procedure as for the Zernike polynomials, although crosstalk between coefficients was much less pronounced, partly due to the higher number of pixels inside the aperture of the lens. The coefficients A_j obtained are listed in Table 2. The structure of the polynomials is such that the ideal line focus lens would only have a contribution for either $j = 4$ or $j = 6$, in the present case, the desired term is the latter. All other contributions are to be seen as aberrations, with three terms exceeding 1% of the magnitude of the desired coefficient. All three larger deviation terms are quadratic in x, indicating an undesired focusing effect in the vertical direction. This can be explained by an inclination of the sidewalls of the lithographic

structures that has been observed in other experiments [15], leading to a variation of the focal length with the height of the structures.

<div align="center">

Table 2. Legendre Coefficients for the Polymer Line Focus Lens

j	Polynomial degree in x	Polynomial degree in y	A_j
4	**2**	**0**	**-3.74**
5	1	1	-0.05
6	**0**	**2**	**-188.0**
7	3	0	0.14
8	**2**	**1**	**-1.99**
9	1	2	-1.52
10	0	3	-0.11
11	4	0	-0.12
12	3	1	0.00
13	**2**	**2**	**2.29**
14	1	3	0.02
15	0	4	0.81

</div>

The data of the phase gradient can provide another quantification of this effect by plotting the focal length of the lens, as determined from the slope of the gradient, over the height of the lens aperture, see Fig. 3. The focal length increases continuously by about 2 m from substrate to top of the lens. This variation corresponds to 1.3% and is thus of the same order of magnitude as the aberration terms obtained via Legendre decomposition. This increase of the parabola apex radius may be due to secondary effects during the exposure step in the lithographic fabrication process, the finite beam divergence in the same step, or shrinkage of the photoresist during the crosslinking process.
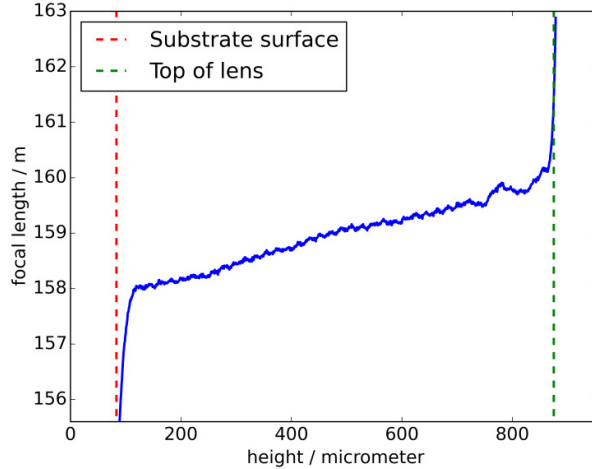

Fig. 3. Profile of the focal length of the polymer line focus length over the height of the aperture.

5. Conclusion and outlook

The single grating, one dimensional X-ray interferometer built for these experiments at the beamline ID06 of the ESRF is a high sensitivity, high resolution tool for routine optics characterization. Full characterization of two types of X-ray lenses was carried out by rotating the samples about the optical axis and acquiring multiple scans to calculate the two

dimensional phase gradient. Local lens defects are quantified by calculating the residuals from a linear fit to the refraction angle throughout the aperture, revealing material inhomogeneities and localized defects in a beryllium point focus lens, while a polymer line focus lens fabricated by X-ray lithography only shows defects with lower spatial frequency, owing to higher material homogeneity.

Global lens aberrations were quantified by retrieving the wavefront phase and decomposing the result in either Zernike respectively Legendre polynomials, depending on the type of lens and aperture shape. All aberrations found were smaller than 1% of the focusing term for the beryllium lens, attesting a high contour accuracy. In the polymer lens, the greatest deviation found is a focusing term in the direction perpendicular to the intended direction amounting to about 2% of the orthogonal focusing term. This indicates a variation of the lens shape along its height, which is also expressed by an increase of the focal length by 1.3% along the lens profile.

These results highlight the individual strengths of the fabrication methods and point out desirable future improvements. The interferometer is equipped for fast sample change and could be used to perform quality control for a complete set of lenses forming a CRL. It can also be operated in a single shot mode to reduce acquisition time by a factor of 16 compared to the results shown here. This comes at the price of reduced resolution and increased crosstalk between coefficients in the polynomial decomposition of the wavefront. To enable the characterization of a large number of samples, it might be preferable to transfer this characterization tool to a laboratory based system with a tube source [16].

Appendix A: Identification of artifacts from oversampling data

As pointed out in section 3, we performed oversampling of azimuthal angles for each lens in order to identify artifacts in the final images. In the polymer lens, concentric circular features reminiscent of ring artifacts in tomography are visible in the angular deviation map (Fig. 4, left). In the lithographic fabrication process, no circular or rotating tools are used, such that the accidental introduction of circular features appears unlikely. Instead, they are more likely to be introduced by the rotation in the data acquisition. This is confirmed when investigating the raw data. Any circular feature of the sample should show up in the 2d phase gradient calculated from any pair of raw images. We see, however, that individual images contain contrast parallel to the grating lines, which could arise from beam or mechanical instabilities. Superposition of many such linear artifacts in rotated images then averages to the observed circular features which are concentric about the rotation axis, as illustrated in Fig. 4.
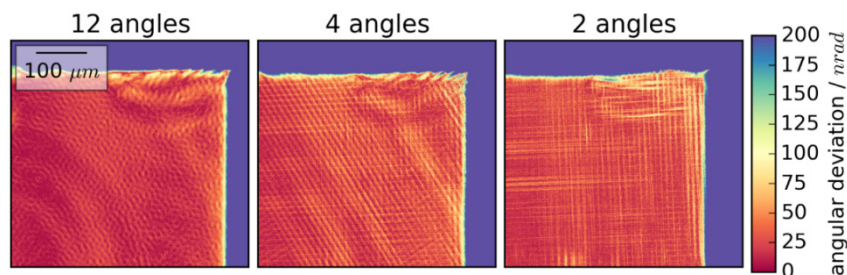

Fig. 4. Magnified area of the angular deviation map of the polymer lens seen in Fig. 2. calculated with (from left to right) 12, 4 and 2 scans at different azimuthal angles.

A second type of artifact originated from a defect in the phase grating. For small refraction angles, defects in the phase grating should not appear in the final image, as they are corrected for with a flat field scan. However, if the refraction angles become large enough to project the grating defect on a different set of pixels on the detector, this correction fails and produces an artifact at both the original and the new position of the grating defect on the detector. This is

visible in Fig. 5, where the upper left quarter of the angular deviation map of the beryllium lens is depicted. In the original map, calculated from ten angular positions, the grating defect appears at four different positions in this quarter, while it appears at only two positions, when using four angles, and only one position when using the minimum of two angles. Note also how the averaging over many angular positions lets the grating defect appear less pronounced but emphasizes other features. The stripes seen in Fig. 4 are less dominant here because the beryllium lens was measured in a lower Talbot order and therefore with lower sensitivity.
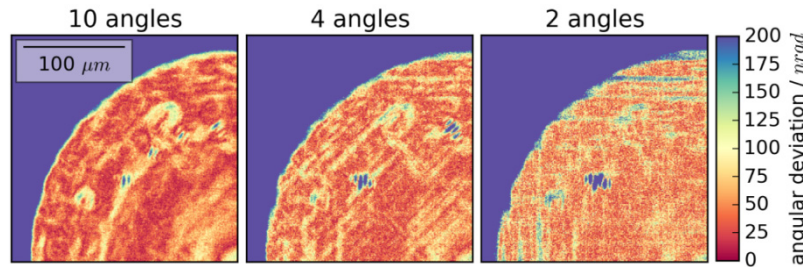

Fig. 5. Magnified area of the angular deviation map of the beryllium lens seen in Fig. 2 calculated with (from left to right) 10, 4 and 2 scans at different azimuthal angles.

Appendix B: quantification of artifact influence on lens characterization

While the previous section explained the shape of artifacts encountered, one can quantify their influence on both local and global characterization of the lens. With the configuration presented here, the standard deviation of the measured refraction angle in areas with no sample was 17 nrad, which means that a strongly localized defect has to cause a deviation greater than this to be reliably identified. Note that the mean deviation of the polymer lens inside the aperture is not greater than that, but the low frequency defects can be identified nevertheless. The cause for this deviation is thought to be mainly mechanical and beam instability, which could be improved in further experiments.

The influence on the characterization of global defects was investigated by modeling the defects and doing a decomposition analogous to the decomposition of the measured wavefront. The circular features seen in the polymer lens were modeled by concentric rings of $+/-$ 15 nrad refraction angle with a width of 30 µm, which corresponds to the experimental values. The largest coefficient found in the decomposition was 0.03 µm, which is insignificant compared to the values obtained for the real lens. The same procedure was used to model the influence of a grating defect as seen in the characterization of the beryllium lens. Here a circle of 20 µm diameter with a refraction angle of 250 nrad was used as model, which represents the artifact seen in Fig. 5 with only 2 images used for reconstruction. The largest coefficient found here is only 0.006 µm, confirming that the decomposition into Zernike polynomials is insensitive to high frequency defects.

Acknowledgments